*Journal of Advanced Ceramics*
2020, **9**(5): 576–587
https://doi.org/10.1007/s40145-020-0396-3

ISSN 2226-4108
CN 10-1154/TQ

**Research Article**

# $Zn^{2+}$ substituted superparamagnetic $MgFe_2O_4$ spinel-ferrites: Investigations on structural and spin-interactions

Lakshita PHOR*, Surjeet CHAHAL, Vinod KUMAR*

*Department of Physics*, *Deenbandhu Chhotu Ram University of Science and Technology*, *Murthal 131039*, *Haryana*, *India*

Received: March 28, 2020; Revised: May 27, 2020; Accepted: June 10, 2020


**Abstract:** Nano-magnetic ferrites with composition $Mg_{1-x}Zn_xFe_2O_4$ ($x$ = 0.3, 0.4, 0.5, 0.6, and 0.7) have been prepared by coprecipitation method. X-ray diffraction (XRD) studies showed that the lattice parameter was found to increase from 8.402 to 8.424 Å with $Zn^{2+}$ ion content from 0.3 to 0.7. Fourier transform infrared (FTIR) spectra revealed two prominent peaks corresponding to tetrahedral and octahedral at around 560 and 430 $cm^{-1}$ respectively that confirmed the spinel phase of the samples. Transmission electron microscopy (TEM) images showed that the particle size was noted to increase from 18 to 24 nm with an increase in Zn content from $x$ = 0.3 to 0.7. The magnetic properties were studied by vibrating sample magnetometer (VSM) and electron paramagnetic resonance (EPR) which ascertained the superparamagnetic behavior of the samples and contribution of superexchange interactions. The maximum magnetization was found to vary from 23.80 to 32.78 emu/g that increased till $x$ = 0.5 and decreased thereafter. Further, X-ray photoelectron spectroscopy (XPS) was employed to investigate the chemical composition and substantiate their oxidation states.

**Keywords:** nanoparticles (NPs); nanospinel ferrites; structural properties; magnetism; coprecipitation method

## 1 Introduction

Nano-spinel ferrites have drawn considerable attention of researchers owing to their fascinating and noticeably distinguishing characteristics than their corresponding bulk part. They have a wide range of applications in diverse fields like memory storage devices, high-density magnetic recording discs, ferrofluids, magnetocaloric refrigeration, hyperthermia, drug delivery, and many other biomedical applications [1–6]. A cubic spinel ferrite possesses a general formula $AB_2O_4$ where A is divalent metal ion like (Mg, Mn, Zn, Ni, etc.). It consists of an FCC lattice of oxygen anions in which metal ions ($M^{2+}$, $Fe^{3+}$) occupy tetrahedral (A) and octahedral (B) sites.

$MgFe_2O_4$ is predominantly an inverse spinel ferrite with $Mg^{2+}$ ions occupying B sites and $Fe^{3+}$ ions distributed over A and B sites with formula unit $(Fe^{3+})_A[Mg^{2+}Fe^{3+}]_BO_4$. However, the degree of inversion depends on the heating effects. On the other hand, $ZnFe_2O_4$ is a typical normal spinel ferrite with formula unit $(Zn^{2+})_A[Fe_2^{3+}]_BO_4$ as $Zn^{2+}$ ions preferentially occupy A sites. Amongst the ferrites investigated, $Mg_{1-x}Zn_xFe_2O_4$ is soft, magnetic, and mixed spinel

* Corresponding authors.
E-mail: L. Phor, lakshitaphor01@gmail.com;
V. Kumar, vinod.phy@dcrustm.org

ferrite, having a variety of applications like catalysis, humidity sensing, magnetic technology, and biomedicine [7,8]. $Mg_{1-x}Zn_xFe_2O_4$ has been reported as a promising candidate for hyperthermia therapy in cancer treatment owing to their appropriate heating effects in response to the alternating magnetic field, chemical stability, biocompatibility, and superparamagnetic properties [9,10]. Moreover, magnesium and zinc are eco-friendly and non-toxic elements, and are essential vital elements found in the human body [11]. Liu *et al*. [12] synthesized $Mg_{1-x}Zn_xFe_2O_4$ nanoparticles by coprecipitation method and studied their structural, magnetic, and thermal properties. They revealed that the AC magnetic field induced heating properties in these materials facilitates their application in hyperthermia treatment. Reyes-Rodríguez *et al*. [13] also developed $Mg_{1-x}Zn_xFe_2O_4$ nanoparticles by sol-gel method and confirmed that nanoparticles can raise the temperature of medium up to 42 ℃ in 10 min. Kassabova-Zhetcheva *et al*. [14] studied the superparamagnetic properties of $Mg_xZn_{1-x}Fe_2O_4$ and their potential application in hyperthermia treatment; however, their heating ability was not estimated. $Mg_{1-x}Zn_xFe_2O_4$ is a high frequency soft magnetic ferrite which is simple and cost-effective. Besides, it is well known that as the substitution of zinc increases and Curie temperature decreases. So, many researchers have emphasized the need for a detailed study of nano-size Mg–Zn ferrites, their superparamagnetic behavior, and the spin-exchange interactions occurring in these materials by which we can well explain the compositional and size dependence of their structural and magnetic properties [15,16].

In the current communication, a detailed investigation has been carried out on the synthesis of superparamagnetic $Mn_{1-x}Zn_xFe_2O_4$ ferrite nanoparticles (NPs) and their characterization for structural and magnetic properties. Their properties are well explained based on results obtained by using analytical techniques viz. X-ray diffraction (XRD) and Fourier transform infrared spectroscopy (FTIR), transmission electron microscopy (TEM), vibrating sample magnetometer (VSM), and electron paramagnetic resonance (EPR).

## 2 Experimental

### 2. 1 Synthesis

$Mg_{1-x}Zn_xFe_2O_4$ ($x$ = 0.3, 0.4, 0.5, 0.6, and 0.7) NPs were synthesized by co-precipitation method using chemical reagents of analytical grade (Sigma Aldrich). Stoichiometric ratio of $Mg(NO_3)_2{\cdot}6H_2O$, $Zn(NO_3)_2{\cdot}9H_2O$, and $Fe(NO_3)_3{\cdot}9H_2O$ was mixed in distilled water individually to get a clear homogenous solution. These solutions were mixed and heated at 60 ℃ under constant stirring. Then, oleic acid was added dropwise to the solution to avoid atmospheric oxidation and agglomeration of particles. With constant heating at 80 ℃ and stirring, the analytical grade ammonia solution was added for the formation of precipitates until the pH was adjusted to 11–12. To transform hydroxides into ferrites, a constant temperature of 85 ℃ was maintained for approximately 1 h. They were then washed with distilled water several times and dried to get NPs.

### 2. 2 Characterization

XRD measurements were carried out by Rigaku Ultima IV Powder XRD with Cu Kα radiations ($\lambda$ = 1.5406 Å) in 2$\theta$ range of 20°–70° with scanning speed of 2 (º)/min. FTIR spectroscopy measurements were done using Perkin Elmer Frontier infrared spectrophotometer by KBr pallet technique in wavenumber range of 4000–400 $cm^{-1}$. Morphology, size, and shape of the samples were analyzed using a cryo-TEM Thermo Scientific Model Talos by dispersing the powder on carbon-coated copper grids. Magnetic properties were investigated by employing Microsense EZ9 VSM at room temperature (RT) in the field range of ±10,000 G. Omicron X-ray photoelectron spectroscopy (XPS) was used to probe the electronic and chemical composition of the samples. EPR spectra were recorded at RT using Bruker Biospin Make, Model A300 at a frequency of 9.85 GHz and modulation frequency of 100 kHz.

## 3 Results and discussion

### 3. 1 XRD analysis

XRD pattern for $Mg_{1-x}Zn_xFe_2O_4$ (0.3, 0.4, 0.5, 0.6, and 0.7) powder confirmed spinel cubic structure for all the samples as shown in Fig. 1. The major peaks corresponded to planes (220), (311), (400), (422), (511), and (440) that matched well with the JCPDS file 00-008-0234 [17]. The crystallite size ($D$) was calculated about the plane (311) corresponding to the peak having maximum intensity using the Scherrer's formula [18]:

$$D = \frac{k\lambda}{\beta \cos\theta_{311}} \quad (1)$$

and experimental lattice parameter ($a_{exp}$) was evaluated using the following equation:

$$a_{exp} = d\sqrt{h^2 + k^2 + l^2} \quad (2)$$

where $k = 0.9$ is shape factor, $d$ is interplanar spacing, $\lambda$ is the wavelength of Cu Kα radiations (1.5406 Å), $\beta$ and $\theta_{311}$ are full width half maxima (FWHM) and Bragg's angle, respectively, corresponding to the plane (311).

Table 1 shows the cation distribution, values of $a_{exp}$ and $D$ for all the samples. It is seen that $Zn^{2+}$ ions exclusively occupy A sites, $Mg^{2+}$ predominantly occupy B sites, a few $Mg^{2+}$ ions migrate to A sites whereas $Fe^{3+}$ ions are distributed over A and B sites. The cation distribution given in Table 1 which is used for the theoretical calculations is obtained based on the Mossbauer study by Mohammed *et al*. [19] while the experimental calculations are made using the XRD pattern obtained in Fig. 1. It is observed that as $Zn^{2+}$ substitution increases from 0.3 to 0.7, $a_{exp}$ values increase from 8.402 to 8.424 Å. This can be explained based on cation radii of ions; $Zn^{2+}$ ions (0.74 Å) have larger ionic radii than $Mg^{2+}$ (0.66 Å) and $Fe^{3+}$ ions (0.67 Å). So, when larger $Zn^{2+}$ replaces smaller $Fe^{3+}$ ions at A sites and pushes the $Fe^{3+}$ ions to replace smaller $Mg^{2+}$ at B sites, then $a_{exp}$ is anticipated to increase. Further, non-linear variation in values of crystallite size can be attributed to the synergic effect between chemical composition and heat treatment [20,21].

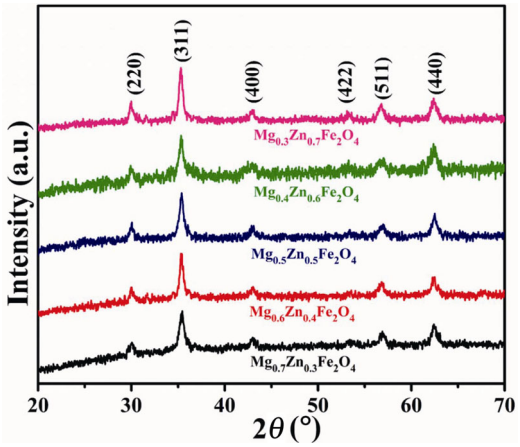


**Fig. 1** XRD patterns for $Mg_{1-x}Zn_xFe_2O_4$ ($x$ = 0.3, 0.4, 0.5, 0.6, and 0.7) NPs.

**Table 1 Cation distribution, $a_{exp}$, and $D$ for $Mg_{1-x}Zn_xFe_2O_4$ ($x$ = 0.3, 0.4, 0.5, 0.6, and 0.7) NPs**

| $x$ | Cation distribution [19] | $a_{exp}$ (Å) | $D$ (nm) |
|---|---|---|---|
| 0.3 | $(Zn^{2+}_{0.3}Mg^{2+}_{0.08}Fe^{3+}_{0.62})^A(Mg^{2+}_{0.62}Fe^{3+}_{1.38})^B$ | 8.402 | 13.32 |
| 0.4 | $(Zn^{2+}_{0.4}Mg^{2+}_{0.07}Fe^{3+}_{0.53})^A(Mg^{2+}_{0.53}Fe^{3+}_{1.47})^B$ | 8.407 | 17.16 |
| 0.5 | $(Zn^{2+}_{0.5}Mg^{2+}_{0.05}Fe^{3+}_{0.45})^A(Mg^{2+}_{0.45}Fe^{3+}_{1.55})^B$ | 8.409 | 15.29 |
| 0.6 | $(Zn^{2+}_{0.6}Mg^{2+}_{0.05}Fe^{3+}_{0.35})^A(Mg^{2+}_{0.35}Fe^{3+}_{1.65})^B$ | 8.415 | 14.75 |
| 0.7 | $(Zn^{2+}_{0.7}Mg^{2+}_{0.04}Fe^{3+}_{0.26})^A(Mg^{2+}_{0.26}Fe^{3+}_{1.74})^B$ | 8.424 | 17.63 |

Using the cation distribution given in Table 1, the average cationic radius at A ($r_A$) and B ($r_B$) sites can be given using Eqs. (3) and (4) [22]:

$$r_A = (C^A_{Mg^{2+}})(r_{Mg^{2+}}) + (C^A_{Zn^{2+}})(r_{Zn^{2+}}) + (C^A_{Fe^{3+}})(r_{Fe^{3+}}) \quad (3)$$

$$r_B = \frac{1}{2}[(C^B_{Mg^{2+}})(r_{Mg^{2+}}) + (C^B_{Zn^{2+}})(r_{Zn^{2+}}) + (C^B_{Fe^{3+}})(r_{Fe^{3+}})] \quad (4)$$

where $C^A$ is ionic concentration for A site and $C^B$ for B sites, respectively, $r_{Fe^{3+}}$, $r_{Mg^{2+}}$, and $r_{Zn^{2+}}$ are radii of $Fe^{3+}$, $Mg^{2+}$, and $Zn^{2+}$ ions, respectively.

Table 2 shows that upon increasing the Zn content, $r_A$ and $r_B$ both increase which can be due to larger $Zn^{2+}$ replacing smaller $Fe^{3+}$ ions at A sites and $Mg^{2+}$ substituted by larger $Fe^{3+}$ ions at B sites as explained above. Theoretical lattice parameter ($a_{th}$) can be calculated by using an oxygen ion radius ($R_O$ = 1.32 Å) using Eq. (5) [23]:

$$a_{th} = 8 \times \frac{r_A + R_0 + \sqrt{3}(r_B + R_0)}{3\sqrt{3}} \quad (5)$$

It is noted that both $a_{exp}$ and $a_{th}$ show an increasing trend with Zn concentration increasing. It is observed that $a_{th}$ shows a more linear trend with increasing Zn content. The difference in the values of $a_{exp}$ and $a_{th}$ can be due to the theoretical calculations considering a closely packed spinel structure. However, each lattice is distorted due to the larger size of cations compared to the tetrahedral and octahedral sites.

Oxygen positional parameter ($U$), which gives the qualitative measurement of displacement of oxygen

**Table 2 $a_{th}$, $r_A$, $r_B$, $U$, and $\delta$ for $Mg_{1-x}Zn_xFe_2O_4$ ($x$ = 0.3, 0.4, 0.5, 0.6, and 0.7) NPs**

| $x$ | $a_{th}$ (Å) | $r_A$ (Å) | $r_B$ (Å) | $U$ | $\delta$ |
|---|---|---|---|---|---|
| 0.3 | 8.3931 | 0.6902 | 0.6669 | 0.3883 | 0.0133 |
| 0.4 | 8.4054 | 0.6973 | 0.6674 | 0.3886 | 0.0136 |
| 0.5 | 8.4174 | 0.7045 | 0.6678 | 0.3889 | 0.0139 |
| 0.6 | 8.4295 | 0.7115 | 0.6683 | 0.3891 | 0.0141 |
| 0.7 | 8.4417 | 0.7186 | 0.6687 | 0.3894 | 0.0144 |

ions concerning A sites and inversion parameter ($\delta$) described as the deviation of $U$ from $U_{ideal}$ (0.375) are given by Eqs. (6) and (7) [24]:

$$U = \left(\frac{1}{a_{th}\sqrt{3}}\right)\left(r_A + R_0\right) + \frac{1}{4} \tag{6}$$

$$\delta = U - 0.375 \tag{7}$$

It is observed from Table 2 that values of $U$ and $\delta$ increase with substitution of $Zn^{2+}$ ions. In this case, as the $x$ value increases, larger $Zn^{2+}$ ions occupy A sites and replace smaller $Mg^{2+}$ and $Fe^{3+}$ ions. This expansion in A sites leads to movement of adjacent oxygen ions, this leads to an increase in $U$. The deviation of $U$ from $U_{ideal}$ is a measure of the effect of trigonal distortion at B sites due to the displacement of oxygen ions. So, an increase in deviation in the present case indicates increasing trigonal distortion at B sites.

Distance between cation–anion at A sites ($R_A$) and B sites ($R_B$) also known as bond lengths can be calculated using Eqs. (8) and (9) [25]:

$$R_A = a\sqrt{3}\left(\delta + \frac{1}{8}\right) \tag{8}$$

$$R_B = a\sqrt{3\delta^2 - \frac{\delta}{2} + \frac{1}{16}} \tag{9}$$

Table 3 shows the variation in values of bond lengths $R_A$ and $R_B$ with Zn substitution. It is noted that $R_A$ values increase while $R_B$ values decrease with increasing $x$. The observed variation can be due to the substitution process: The substitution of $Zn^{2+}$ ions with larger ionic radius causes expansion at A sites, and hence the $R_A$ increases. This displacement in oxygen ions away from A sites (towards B sites) results in shrinkage of B sites. Hence, $R_B$ decreases [19]. Further, values of $R_A$ are higher than $R_B$ which can be explained as the covalent bonding of $Fe^{3+}$ ions at B sites is more than at A sites. Hence, the results are in good agreement with the explanation that relates to the increase in covalent bonding with a decrease in bond length [26].

The tetrahedral edge length ($R_X$), shared octahedral edge length ($R'_X$), and unshared octahedral edge length ($R''_X$) are calculated using Eqs. (10)–(12) [19]:

$$R_X = a\sqrt{2}\left(2U - \frac{1}{2}\right) \tag{10}$$

$$R'_X = a\sqrt{2}(1 - 2U) \tag{11}$$

$$R''_X = a\sqrt{4U^2 - 3U + \frac{11}{16}} \tag{12}$$

**Table 3 $R_A$, $R_B$, $R_X$, $R'_X$, and $R''_X$ for $Mg_{1-x}Zn_xFe_2O_4$ ($x$ = 0.3, 0.4, 0.5, 0.6, and 0.7) NPs**

| $x$ | $R_A$ (Å) | $R_B$ (Å) | $R_X$ (Å) | $R'_X$ (Å) | $R''_X$ (Å) |
|---|---|---|---|---|---|
| 0.3 | 2.0126 | 1.9951 | 3.2862 | 2.6542 | 2.9791 |
| 0.4 | 2.0182 | 1.9941 | 3.2953 | 2.6487 | 2.9812 |
| 0.5 | 2.0229 | 1.9921 | 3.3029 | 2.6419 | 2.9821 |
| 0.6 | 2.0274 | 1.9922 | 3.3102 | 2.6392 | 2.9846 |
| 0.7 | 2.0339 | 1.9921 | 3.3210 | 2.6349 | 2.9883 |

It is clear that as Zn concentration increased, $R_X$ and $R''_X$ values increased due to their dependence on lattice parameter. However, the decrease in $R'_X$ values with $x$ can be due to distortion of B sites symmetry as a result of variation in $U$ that causes anions to come close to the edge and hence reducing the B shared edge length [27].

The distance between cation–anion ($p$, $q$, $r$, and $s$), cation–cation ($b$, $c$, $d$, $e$, and $f$), and the angle between them in spinel ferrites are shown in Fig. 2 and evaluated using Eqs. (13)–(21) [28].

$$p = a\left(\frac{5}{8} - U\right) \tag{13}$$

$$q = a\left(U - \frac{1}{4}\right)\sqrt{3} \tag{14}$$

$$r = a\left(U - \frac{1}{4}\right)\sqrt{11} \tag{15}$$

$$s = a\left(\frac{1}{3}U + \frac{1}{8}\right)\sqrt{3} \tag{16}$$

$$b = \left(\frac{a}{4}\right)\sqrt{2} \tag{17}$$

$$c = \left(\frac{a}{8}\right)\sqrt{11} \tag{18}$$

$$d = \left(\frac{a}{4}\right)\sqrt{3} \tag{19}$$

$$e = \left(\frac{3a}{8}\right)\sqrt{3} \tag{20}$$

$$f = \left(\frac{a}{4}\right)\sqrt{6} \tag{21}$$

Table 4 shows that all cation–anion and cation–cation distances (except $p$) show an increasing trend with Zn doping as the values of these parameters depend on the experimental lattice parameter and oxygen positional parameter [19]. These interionic distances

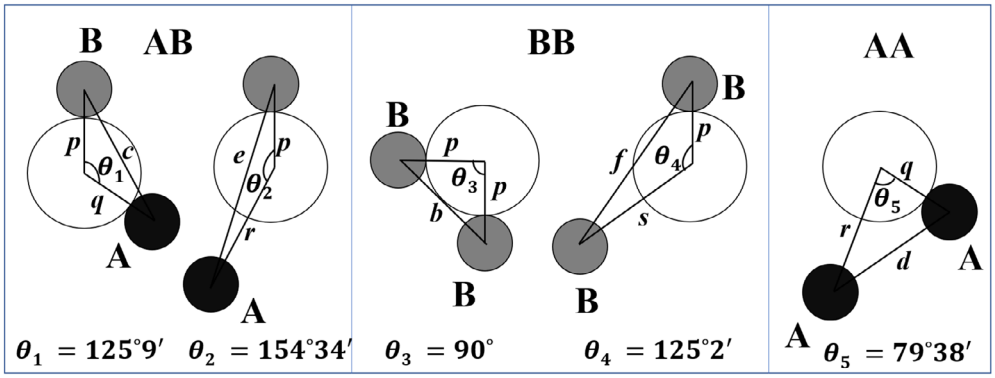


**Fig. 2** Distance and angles between cation–cation and cation–anion at A and B sites.

**Table 4 Cation–anion distances (*p*, *q*, *r*, *s*) and cation–cation distances (*b*, *c*, *d*, *e*, *f*) for $Mg_{1-x}Zn_xFe_2O_4$ (*x* = 0.3, 0.4, 0.5, 0.6, and 0.7) NPs**

| *x* | *p* (Å) | *q* (Å) | *r* (Å) | *s* (Å) | *b* (Å) | *c* (Å) | *d* (Å) | *e* (Å) | *f* (Å) |
|---|---|---|---|---|---|---|---|---|---|
| 0.3 | 1.9888 | 2.0126 | 3.8539 | 3.6839 | 2.9706 | 3.4834 | 3.6383 | 5.4575 | 5.1453 |
| 0.4 | 1.9875 | 2.0182 | 3.8647 | 3.6876 | 2.9724 | 3.4855 | 3.6405 | 5.4608 | 5.1485 |
| 0.5 | 1.9853 | 2.0229 | 3.8737 | 3.6895 | 2.9723 | 3.4860 | 3.6410 | 5.4615 | 5.1492 |
| 0.6 | 1.9851 | 2.0274 | 3.8823 | 3.6933 | 2.9754 | 3.4887 | 3.6438 | 5.4657 | 5.1531 |
| 0.7 | 1.9845 | 2.0339 | 3.8947 | 3.6988 | 2.9784 | 3.4925 | 3.6478 | 5.4717 | 5.1587 |

can be further used to calculate bond angles using the following Eqs. (22)–(26) [27,29]:

$$\theta_1 = \cos^{-1}\left(\frac{p^2+q^2-c^2}{2pq}\right) \quad (22)$$

$$\theta_2 = \cos^{-1}\left(\frac{p^2+r^2-e^2}{2pr}\right) \quad (23)$$

$$\theta_3 = \cos^{-1}\left(\frac{2p^2-b^2}{2p^2}\right) \quad (24)$$

$$\theta_4 = \cos^{-1}\left(\frac{p^2+s^2-f^2}{2ps}\right) \quad (25)$$

$$\theta_5 = \cos^{-1}\left(\frac{r^2+q^2-d^2}{2rq}\right) \quad (26)$$

The variation in the values of bond angles with $Zn^{2+}$ ion content is shown in Table 5. The increasing angle values refer to the strengthening of corresponding cation–cation or cation–anion interaction decrease indicate weakening of the concerned interactions. It is observed that the angles $\theta_3$ and $\theta_4$ increased while $\theta_1$, $\theta_2$, and $\theta_5$ decreased with increasing *x* in $Mg_{1-x}Zn_xFe_2O_4$ (*x* = 0.3, 0.4, 0.5, 0.6, and 0.7) indicating strong A–B interactions, and weak B–B interactions, respectively [27].

**Table 5 Interionic angles for $Mg_{1-x}Zn_xFe_2O_4$ (*x* = 0.3, 0.4, 0.5, 0.6, and 0.7) NPs**

| *x* | $\theta_1$ (°) | $\theta_2$ (°) | $\theta_3$ (°) | $\theta_4$ (°) | $\theta_5$ (°) |
|---|---|---|---|---|---|
| 0.3 | 121.0430 | 135.7288 | 96.6334 | 127.6354 | 68.5776 |
| 0.4 | 120.9468 | 135.3788 | 96.7958 | 127.6734 | 68.2886 |
| 0.5 | 120.8487 | 135.0267 | 96.9191 | 127.7092 | 68.1187 |
| 0.6 | 120.7878 | 134.8006 | 97.0860 | 127.7318 | 67.9675 |
| 0.7 | 120.7098 | 134.4889 | 97.2528 | 127.7754 | 67.7495 |

### 3.2 FTIR spectroscopy analysis

FTIR is a remarkable spectroscopic technique that helps to estimate the formation of cubic spinel phase and probe the various functional groups present in the samples. Waldron [30] asserted that ferrites can be characterized by vibrational frequencies referred to as $\nu_1$, $\nu_2$, $\nu_3$, and $\nu_4$. Frequencies $\nu_1$ and $\nu_2$ correspond to the intrinsic stretching vibrations of $Fe^{3+}$–$O^{2-}$ at A sites around 600–500 $cm^{-1}$ and B sites 450–350 $cm^{-1}$, respectively. Moreover, $\nu_3$ and $\nu_4$ occur at small frequencies and attributed to the metal ions vibrations at A sites or B sites.

Figure 3 shows the FTIR spectrum for $Mg_{1-x}Zn_xFe_2O_4$ samples at RT in the range of 4000–400 $cm^{-1}$. The variation in the vibrational frequencies at A sites ($\nu_1$) and B sites ($\nu_2$) with an increase in Zn content is tabulated in Table 6. It can be noted that $\nu_1$ is higher

than $\nu_2$ due to additional overlapping of $Fe^{3+}$–$O^{2-}$ at A sites than B sites. Since the position of these two absorption bands depends upon the difference in the distances of $Fe^{3+}$–$O^{2-}$ for A and B sublattices. Further, a decrease in values of $\nu_1$ with an increase in substitution of $Zn^{2+}$ ions can be attributed to the increase in cation-oxygen bond length at A site that corroborates well with XRD results. It can be understood based on the weakening of metal–oxygen bond due to substitution of $Zn^{2+}$ ions at A sites causing migration of equivalent $Fe^{3+}$ ions from A to B sites. It is also observed that position of $\nu_2$ shifts towards higher wavenumber range. This implies the strengthening of the metal–oxygen bond as a result of the immigration of $Fe^{3+}$ ions to B sites. The results reported by Chhantbar *et al*. [31,32] agree to some extent with the present case. It can be clearly seen that wavenumbers corresponding to vibrational frequency $\nu_3$ and $\nu_4$ lie outside the measurement range. Further, it is well known that vibrational frequency and bond length share an inverse relationship which explains the decrease in vibrational frequency $\nu_1$ and increase in $\nu_2$ values with an increase in Zn content.

Force constant ($F$) measures the strength of the chemical bond that increases with bond order. As the bond length increases, repulsive forces among the concerning ions weaken, resulting in reduced force constant values. Force constants of ions corresponding to A sites ($K_T$) and B sites ($K_O$) can be calculated by inserting the values of vibrational frequencies $\nu_1$ and $\nu_2$ respectively in the following formula:

$$F = 4\pi^2 c^2 \nu^2 m \tag{27}$$

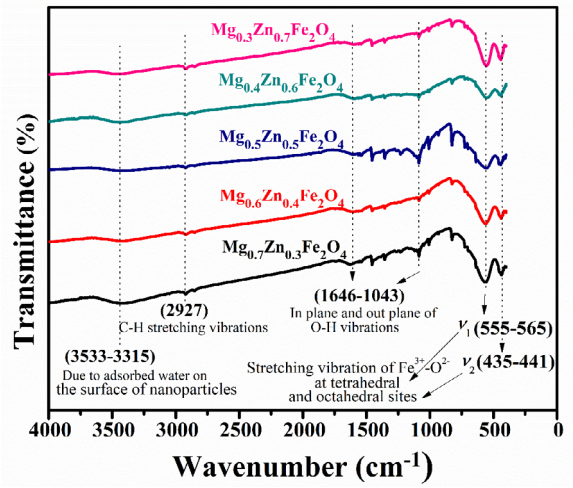


**Fig. 3** FTIR spectra of $Mg_{1-x}Zn_xFe_2O_4$ ($x$ = 0.3, 0.4, 0.5, 0.6, and 0.7) NPs.

**Table 6 Variations in $\nu_1$ and $\nu_2$ and $K_T$ and $K_O$ with $x$ in $Mg_{1-x}Zn_xFe_2O_4$ ($x$ = 0.3, 0.4, 0.5, 0.6, and 0.7) NPs**

| $x$ | $\nu_1$ ($cm^{-1}$) | $\nu_2$ ($cm^{-1}$) | $K_T$ ($10^5$ dyne/cm) | $K_O$ ($10^5$ dyne/cm) |
|---|---|---|---|---|
| 0.3 | 565 | 435 | 2.94721 | 1.747 |
| 0.4 | 562 | 438 | 2.91591 | 1.771 |
| 0.5 | 559 | 439 | 2.88486 | 1.779 |
| 0.6 | 556 | 440 | 2.85398 | 1.787 |
| 0.7 | 554 | 441 | 2.83348 | 1.796 |

where $c$ is the speed of light ($3\times10^{10}$ cm/s), $v$ is the vibrational frequency at A and B sites, and $m$ is the reduced mass of $Fe^{3+}$ and $O^{2-}$ ($2.601\times10^{-23}$ g).

Values of force constants $K_T$ and $K_O$ are summarized in Table 6. It is noted that $K_T$ values decrease with an increase in Zn content. This is understood as: If the substituted ion has a larger ionic radius than the replaced one then cation-oxygen bond lengths at that site increase and consequently force constant decreases. Since, lesser energy is required to break the longer bonds. On the other hand, $K_O$ values increase as Zn content increases due to the movement of $O^{2-}$ ions towards $Fe^{3+}$ ions at B sites as a result of charge imbalance caused by the migration of $Fe^{3+}$ ions from A sites to B sites. This movement leads to a decrease in bond length and hence, an increase in force constant $K_O$ [33]. The broad absorption band observed in the range of 3250–3591 $cm^{-1}$ was assigned to the presence of adsorbed water on the surface of NPs [34,35]. Band at 2927 $cm^{-1}$ refers to the presence of C–H stretching vibrations in all the samples due to the use of KBr while making pallets [36]. Bands at approximately 1696–1391 and 1091–826 $cm^{-1}$ correspond to in-plane and out-plane of O–H vibrations, respectively [37].

### 3.3 TEM analysis

Figure 4 shows the TEM images of $Mg_{1-x}Zn_xFe_2O_4$ ($x$ = 0.3, 0.5, and 0.7) NPs. It has been observed that most of the particles are spherical and agglomerated. Further, it is also noted that the particle size increases as 18, 22, and 24 nm with Zn concentration 0.3, 0.5, and 0.7, respectively, owing to the larger size of the Zn ions than replaced smaller Mg ions.

### 3.4 VSM analysis

The hysteresis loop for $Mg_{1-x}Zn_xFe_2O_4$ ($x$ = 0.3, 0.4, 0.5, 0.6, and 0.7) at RT is shown in Fig. 5. Variation of maximum magnetization ($M_{Max}$), coercivity ($H_C$), retentivity ($M_R$), anisotropy constant ($K$), squareness

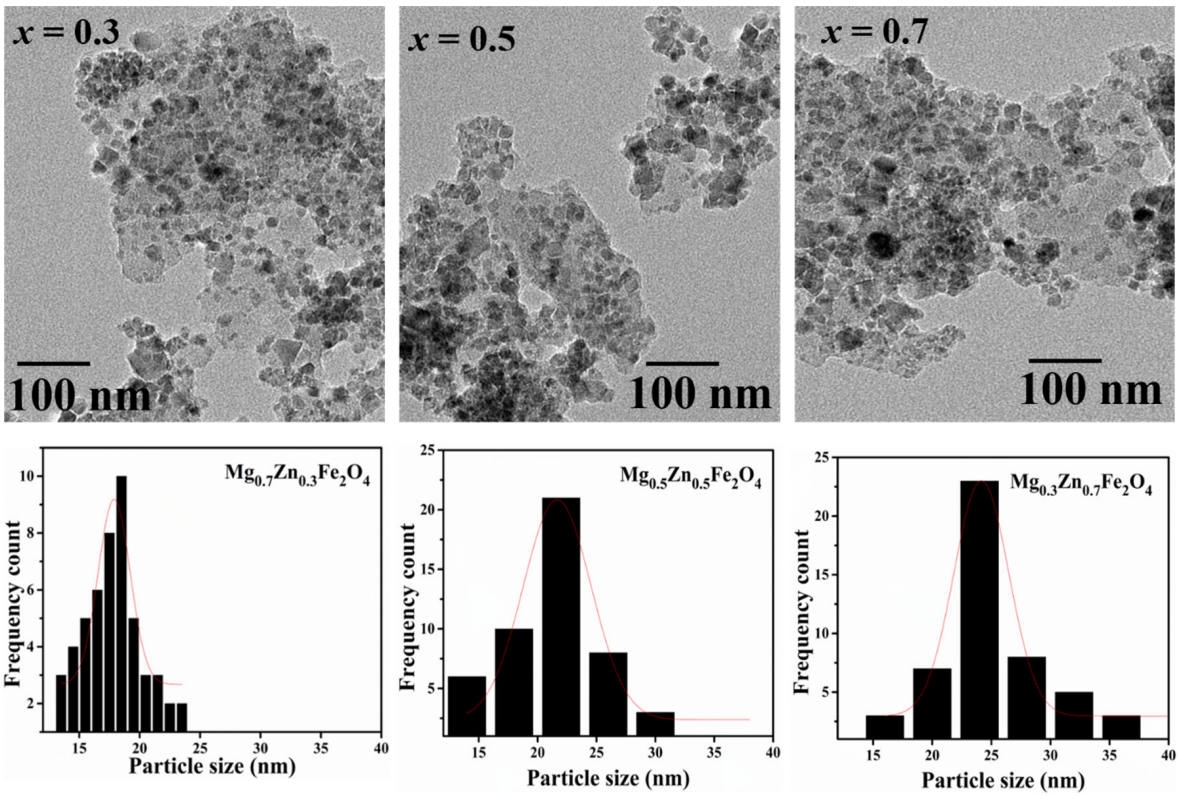


**Fig. 4** TEM images and histograms of $Mg_{1-x}Zn_xFe_2O_4$ NPs.

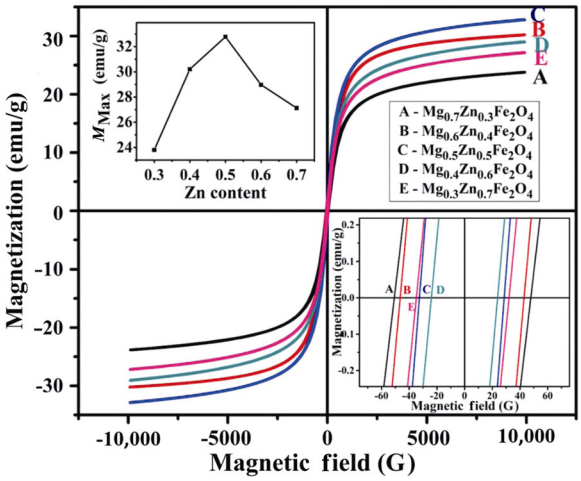


**Fig. 5** Magnetization versus magnetic field curves at RT for $Mg_{1-x}Zn_xFe_2O_4$ NPs; the inset at the top shows the variation of $M_{Max}$ with the Zn content and the inset at the bottom shows coercivity.

(*S*), and magnetic moment ($\eta_B$) have been calculated using Eqs. (28)–(30) [27,38].

$$K = \frac{H_C M_{Max}}{0.96} \tag{28}$$

$$S = \frac{M_R}{M_{Max}} \tag{29}$$

$$\eta_B = \frac{MW \times M_{Max}}{5585} \tag{30}$$

where *MW* is molecular weight, and 5585 is magnetic factor.

It is observed that $M_{Max}$ value increases to $x = 0.5$ and then starts to decrease. The reason for such variation in $M_{Max}$ value can be due to the cation redistribution over A and B sites. In $Mg_{1-x}Zn_xFe_2O_4$, both $Mg^{2+}$ and $Zn^{2+}$ are diamagnetic and hence, non-magnetic. So, their net magnetization depends upon the distribution of $Fe^{3+}$ ions over A and B sites. The resultant magnetization for oppositely magnetized A and B sublattices is given by

$$|M_S| = |M_B - M_A| \tag{31}$$

where $M_S$ stands for saturation magnetization, $M_B$ and $M_A$ denote the magnetic moments at A and B sites, respectively.

$MgFe_2O_4$ ($x = 0$) is an inverse spinel ferrite with $Mg^{2+}$ ions on B sites and $Fe^{3+}$ ions on A and B sites. However, there can be a possibility of a small number of "*x*" $Mg^{2+}$ ions migrating to A sites [39]. The cation distribution may be given as

$$(Mg_x^{2+}Fe_{1-x}^{3+})[Mg_{1-x}^{2+}Fe_{1+x}^{3+}]O_4^{2-} \tag{32}$$

where the curved brackets represent A sublattices and square bracket B sublattices, respectively.

With the substitution of "*y*" $Zn^{2+}$ for $Mg^{2+}$ ions, where $Zn^{2+}$ ions have a strong preference for A site, $Fe^{3+}$ ions are pushed from A to B sites. This causes the magnetization of A sites to decrease due to a reduction in $Fe^{3+}$ ions and the magnetization of B site increases. Therefore, the net magnetization increases till $x = 0.5$. The cation distribution can be modified as

$$(Zn_y^{2+}Mg_x^{2+}Fe_{1-x-y}^{3+})[Mg_{1-x-y}^{2+}Fe_{1+x+y}^{3+}]O_4^{2-} \quad (33)$$

Further, when the content of $Zn^{2+}$ increased more than $x = 0.5$, the net magnetization starts to decrease because then, the fewer $Fe^{3+}$ ions on A site are not anymore able to align the magnetic moments of ions on B site antiparallel to themselves due to negative B–B interactions [40].

In addition, $S$ is a characteristic parameter for magnetic materials that determines whether intergrain exchange interaction exists between NPs or not. Stoner and Wohlfarth [41] asserted that $S = 0.5$ refers to non-interacting randomly oriented NPs whereas $S < 0.5$ to magnetostatic interaction between the particles. It can be clearly seen from Table 7 that $S$ is less than 0.5 for all the compositions. The decrease in coercivity with Zn content can be attributed to the conversion of a single domain to multidomain as the particle size increases [17,42]. However, in parallel to the role of particle size, anisotropy also plays an important role in the value of coercivity and for the sample with $x = 0.7$, the shape anisotropy is higher, due to which these particles have higher values of coercivity [43].

### 3. 5 EPR analysis

EPR is an outstanding spectroscopic technique to examine the dynamical magnetic properties at higher frequencies. Magnetic parameters like super-exchange interactions, magnetic anisotropy, spin–spin relaxation, and dipolar interactions govern the magnetic behavior of NPs which are in turn explained by studying the Lande's g-factor, resonance field ($H_r$), and linewidth ($\Delta H_{PP}$) [44–46]. The EPR spectrum measurements for $Mg_{1-x}Zn_xFe_2O_4$ ferrite NPs were made at a constant microwave frequency of 9.8 GHz in the field range of 0–10,000 G at RT. Figure 6 shows the first derivate of intensity ($I$) versus field ($H$). It is observed that all samples exhibit a symmetrical broad single resonance signal indicating that $Mg^{2+}$, $Zn^{2+}$, and $Fe^{3+}$ ions coexist. The values of g-factor, relaxation time ($T_2$), and spin concentration ($N_S$) have been calculated using $H_r$ and $\Delta H_{PP}$ in the following Eqs. (34)–(37):

$$g = \frac{h\nu}{\mu_B \times H_r} \quad (34)$$

$$N_S = \frac{9\Delta H_{1/2}}{4\pi^2 g \mu_B} \quad (35)$$

$$\Delta H_{1/2} = \sqrt{3}\Delta H_{PP} \quad (36)$$

$$T_2 = \frac{h}{2\pi g \mu_B \Delta H_{1/2}} \quad (37)$$

where $h$ is the Plank's constant ($6.626 \times 10^{-34}$ J·s), $\nu$ is the electromagnetic radiation frequency, $\mu_B$ is the Bohr magneton ($9.27 \times 10^{-24}$ J/T), and $\Delta H_{1/2}$ is the linewidth corresponding to height half of absorption peak.

Table 8 summarizes the estimated values of various EPR parameters. The g-factor values are observed to

**Table 7** $M_{Max}$, $H_C$, $M_R$, $K$, $S$, and $\eta_B$ calculated for $Mg_{1-x}Zn_xFe_2O_4$ ($x = 0.3$, 0.4, 0.5, 0.6, and 0.7) NPs

| $x$ | 0.3 | 0.4 | 0.5 | 0.6 | 0.7 |
|---|---|---|---|---|---|
| $M_{Max}$ (emu/g) | 23.80 | 30.21 | 32.78 | 28.97 | 27.12 |
| $H_C$ (G) | 51 | 46 | 31 | 23 | 35 |
| $M_R$ (emu/g) | 1.6 | 1.9 | 1.5 | 1.0 | 1.4 |
| $K$ (erg/Oe) | 1257.63 | 1467.86 | 1050.73 | 667.41 | 956.08 |
| $S$ | 0.069 | 0.064 | 0.046 | 0.033 | 0.051 |
| $\eta_B$ (μB) | 0.905 | 1.171 | 1.294 | 1.165 | 1.111 |

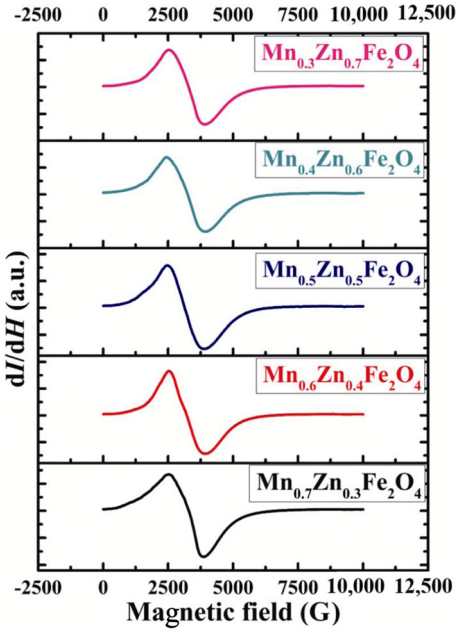


**Fig. 6** Variation of (d$I$/d$H$) with magnetic field for $Mg_{1-x}Zn_xFe_2O_4$ ($x = 0.3$, 0.4, 0.5, 0.6, and 0.7) NPs.

**Table 8 Variation of g-factor, $\Delta H_{PP}$, $H_r$, $N_S$, and $T_2$ for $Mg_{1-x}Zn_xFe_2O_4$ ($x$ = 0.3, 0.4, 0.5, 0.6, and 0.7) NPs**

| $x$ | g-factor | $H_r$ (G) | $\Delta H_{PP}$ (G) | $N_S$ ($10^{21}$) | $T_2$ ($10^{-11}$ s) |
|---|---|---|---|---|---|
| 0.3 | 2.13 | 3295 | 1389 | 2.7861 | 2.2252 |
| 0.4 | 2.18 | 3218 | 1395 | 2.7323 | 2.1642 |
| 0.5 | 2.24 | 3134 | 1453 | 2.7724 | 2.0233 |
| 0.6 | 2.16 | 3250 | 1405 | 2.7789 | 2.1705 |
| 0.7 | 2.13 | 3289 | 1387 | 2.7764 | 2.2248 |

increase from 2.13 to 2.24 with $Zn^{2+}$ content up to $x$ = 0.5 and then decrease. The variation of $H_r$ and $\Delta H_{PP}$ with Zn content in samples is revealed in Fig. 6 and $H_r$ is found to lie between 3134 and 3295 G and $\Delta H_{PP}$ from 1387 to 1453 G. $N_S$ varies from $2.7323 \times 10^{21}$ to $2.7861 \times 10^{21}$ and $T_2$ which measures energy absorption rate that varies from $2.0233 \times 10^{-11}$ to $2.2252 \times 10^{-11}$ s.

It is noted that $\Delta H_{PP}$ and magnetic moment/$M_{Max}$ show the same trend with Zn concentration as shown in Fig. 6. According to the equation modified by Schlomann [47,48], field contributing to the line broadening can arise from various factors such as anisotropy ($H_a$), porosity ($H_p$), eddy currents ($H_e$), and inhomogeneous demagnetization ($H_{id}$):

$$H = -\frac{2K}{M_S} + 4\pi M_S \frac{p}{1-p} + H_e + H_{id} \quad (38)$$

Srivastava and Patin [49] also investigated the linewidth contribution from the aforementioned factors on Ni–Zn and Mg–Mn ferrites and noted that $M_S$ plays an important role in influencing the linewidth and $H_r$. $H_r$ is a fundamental intrinsic property that depends on the internal field, which is further influenced by cation distribution, dipolar interactions, and superexchange interactions. Further, the variation in values of $\Delta H_{PP}$ and g-factor is due to the influence of magnetic dipolar interactions and superexchange interactions between the particles. Since, the magnetization is noted to increase with $Zn^{2+}$ ions due to the strengthening of superexchange interactions between sublattices A and B via $O^{2-}$ ions. Consequently, the first term in Eq. (38) becomes very small, and the second term dominates. At $x$ = 0.5, magnetization has the maximum value and hence, $\Delta H_{PP}$ and g-factor are the maximum. On further increase of Zn substitution, $M_{Max}$ decreases, and anisotropy term dominates resulting in lowering of $\Delta H_{PP}$ values. Priyadarshini *et al*. [35] reported a similar increase in linewidth with saturation magnetization for Ni–Zn ferrites. Moreover, the linewidth is also considered to be a measure of field inhomogeneity in the material, and a decrease in $\Delta H_{PP}$ values after $x$ = 0.5 can be due to the improved magnetic homogeneity in the particles [36,44]. Table 8 shows the experimental values of the magnetic moment ($\mu_B$) and noted to increase with Zn substitution till $x$ = 0.5. Thus, the addition of $Zn^{2+}$ ions causes strengthening of superexchange interactions that contribute to the enhancement in the internal field and consequently decrease in $H_r$. Spin relaxation is a process of transfer of energy difference ($\Delta E$) to adjacent electrons and the variance of $T_2$ that determines the relaxation process and rate of absorption of energy [36]. $T_2$ for all the compositions is mentioned in Table 8 and plays a vital role in restricting the linewidth. Moreover, the trend of $T_2$ is observed to be inverse to that of $\Delta H_{PP}$.

### 3.6 XPS analysis

XPS is a versatile technique that is helpful in probing the elemental composition and their chemical/oxidation states. A survey scan of synthesized $Mg_{0.5}Zn_{0.5}Fe_2O_4$ samples was obtained that confirmed the presence of Mg, Zn, Fe, and O species. High-resolution scan for Fe 2p, O 1s, Mg 2p, and Zn 2p was performed for further analysis (Table 9). Carbon correction has been done using binding energy (284.6 eV) of C 1s before examining the data.

Fe 2p spectra in Fig. 7 have been deconvolved in five peaks of Fe $2p_{3/2}$ and Fe $2p_{1/2}$. Fe $2p_{3/2}$ peak intensity is higher than that of Fe $2p_{1/2}$ due to spin-orbit coupling (j–j). A satellite peak is present at 715.38 eV separating Fe $2p_{3/2}$ and Fe $2p_{1/2}$ peaks that confirm the

**Table 9 Peak positions of fitted of Fe 2p, O 1s, Mg 2p, and Zn 2p spectra of $Mg_{1-x}Zn_xFe_2O_4$ ($x$ = 0.3, 0.4, 0.5, 0.6, and 0.7) NPs**

| Peak | Peak position (eV) |
|---|---|
| Fe 2p | 708.53 |
| | 711.86 |
| | 715.38 |
| | 722.05 |
| | 730.21 |
| O 1s | 529.46 |
| | 530.80 |
| Mg 2p | 54.50 |
| | 49.30 |
| Zn 2p | 1021.39 |
| | 1044.45 |

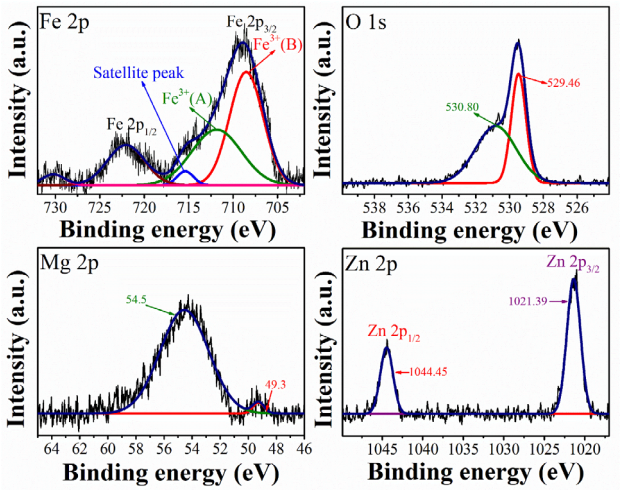


**Fig. 7** XPS spectra for Fe 2p, O 1s, Mg 2p, and Zn 2p of $Mg_{1-x}Zn_xFe_2O_4$ ($x$ = 0.3, 0.4, 0.5, 0.6, and 0.7) NPs.

presence of $Fe^{3+}$ ions corroborating well with XRD results [50]. Deconvolution of Fe $2p_{3/2}$ peak in $Fe^{3+}$(B) and $Fe^{3+}$(A) peaks revealed the existence of $Fe^{3+}$ ions at B and A sites respectively as a result of partial-inversion of the spinel structure [51,52]. O 1s spectra deconvolved in two peaks at 530.8 and 529.46 eV that show the contribution of oxygen in different environments. The peak at 529.46 eV appears due to metal–oxygen bonding and the peak at 530.8 eV can be ascribed to oxygen vacancies or metal-hydroxyl bonds at the surface. Mg 2p signal reveals that the spectrum is composed of two bands located at 49.3 and 54.5 eV. The peak at lower binding energy corresponds to $Mg^{2+}$ ions at A site that shows the presence of a very small fraction of $Mg^{2+}$ ions. The intense peak at 54.5 eV ascribed the presence of $Mg^{2+}$ ions at B site in a large amount. The fitting of Zn 2p spectra in two signals corresponds to Zn $2p_{1/2}$ (1044.45 eV) and Zn $2p_{3/2}$ (1021.39 eV). The spin-orbit splitting energy is found to be 23.06 eV which is in good agreement with some previous results [53,54].

## 4 Conclusions

$Mg_{1-x}Zn_xFe_2O_4$ ($x$ = 0.3, 0.4, 0.5, 0.6, and 0.7) NPs have been successfully synthesized by co-precipitation method. XRD analysis confirmed the spinel cubic structure for all the samples. Effects of Zn content on the various structural parameters like lattice parameter, crystallite size, bond length, and angle have been investigated based on the proposed cation distribution and compared with the theoretically predicted ones. Lattice parameter was found to increase from 8.402 to 8.424 Å with the substitution of $Zn^{2+}$ ions owing to the larger ionic radius of $Zn^{2+}$ ions than $Mg^{2+}$ and $Fe^{3+}$ ions. FTIR studies revealed the stretching vibrational bands at A and B sites and their corresponding force constants. The observed behavior/trend was explained based on bond length (metal–oxygen) and charge imbalance at respective sites. TEM images showed that particle size increased from 18 to 24 nm with Zn substitution which corroborates well with XRD results. Magnetic studies by VSM revealed that the maximum magnetization and magnetic moment increases up to $x$ = 0.5 and decreases thereafter with the addition of $Zn^{2+}$ ions. The values of $H_C$ and $M_R$ were observed to be negligibly small indicating the superparamagnetic behavior of the synthesized NPs. EPR spectra revealed that the variation in values of g-factor and $\Delta H_{PP}$ was attributed to the contribution of superexchange and dipolar interactions and was found to match well with the VSM results. XPS analysis was used to study the chemical composition and their oxidation states.

## Acknowledgements

We are thankful to Thapar Institute of Engineering & Technology for providing a vibrating sample magnetometer facility.

## References

[1] Singh SB, Srinivas C, Tirupanyam BV, *et al*. Structural, thermal and magnetic studies of $Mg_xZn_{1-x}Fe_2O_4$ nanoferrites: Study of exchange interactions on magnetic anisotropy. *Ceram Int* 2016, **42**: 19179–19186.

[2] Srinivas C, Tirupanyam BV, Meena SS, *et al*. Structural and magnetic characterization of co-precipitated $Ni_xZn_{1-x}Fe_2O_4$ ferrite nanoparticles. *J Magn Magn Mater* 2016, **407**: 135–141.

[3] Rahman S, Nadeem K, Anis-Ur-rehman M, *et al*. Structural and magnetic properties of ZnMg-ferrite nanoparticles prepared using the co-precipitation method. *Ceram Int* 2013, **39**: 5235–5239.

[4] Ghatak S, Sinha M, Meikap AK, *et al*. Electrical transport behavior of nonstoichiometric magnesium–zinc ferrite. *Mater Res Bull* 2010, **45**: 954–960.

[5] Niaz Akhtar M, Yahya N, Sattar A, *et al*. Investigations of structural and magnetic properties of nanostructured $Ni_{0.5+x}Zn_{0.5-x}Fe_2O_4$ Magnetic feeders for CSEM application. *Int J Appl Ceram Technol* 2015, **12**: 625–637.

[6] Chahal S, Gaba S, Kumar A, *et al*. Effect of $Mg^{2+}$ substitution on structural and magnetic properties of nano

zinc ferrite. *AIP Conf Proc* 2018, **2006**: 030014.

[7] Shultz MD, Calvin S, Fatouros PP, *et al*. Enhanced ferrite nanoparticles as MRI contrast agents. *J Magn Magn Mater* 2007, **311**: 464–468.

[8] Šepelák V, Bergmann I, Menzel D, *et al*. Magnetization enhancement in nanosized $MgFe_2O_4$ prepared by mechanosynthesis. *J Magn Magn Mater* 2007, **316**: e764–e767.

[9] Ghosh R, Pradhan L, Devi YP, *et al*. Induction heating studies of $Fe_3O_4$ magnetic nanoparticles capped with oleic acid and polyethylene glycol for hyperthermia. *J Mater Chem* 2011, **21**: 13388.

[10] Jadhav NV, Prasad AI, Kumar A, *et al*. Synthesis of oleic acid functionalized $Fe_3O_4$ magnetic nanoparticles and studying their interaction with tumor cells for potential hyperthermia applications. *Colloids Surfaces B: Biointerfaces* 2013, **108**: 158–168.

[11] Masina P, Moyo T, Abdallah HMI. Synthesis, structural and magnetic properties of $Zn_xMg_{1-x}Fe_2O_4$ nanoferrites. *J Magn Magn Mater* 2015, **381**: 41–49.

[12] Liu HY, Li AM, Ding XX, *et al*. Magnetic induction heating properties of $Mg_{1-x}Zn_xFe_2O_4$ ferrites synthesized by co-precipitation method. *Solid State Sci* 2019, **93**: 101–108.

[13] Reyes-Rodríguez PY, Cortés-Hernández DA, Escobedo-Bocardo JC, *et al*. Structural and magnetic properties of Mg–Zn ferrites ($Mg_{1-x}Zn_xFe_2O_4$) prepared by sol-gel method. *J Magn Magn Mater* 2017, **427**: 268–271.

[14] Kassabova-Zhetcheva V, Pavlova L, Samuneva B, *et al*. Characterization of superparamagnetic $Mg_xZn_{1-x}Fe_2O_4$ powders. *Open Chem* 2007, **5**: 107–117.

[15] Khot SS, Shinde NS, Ladgaonkar BP, *et al*. Magnetic and structural properties of magnesium zinc ferrites synthesized at different temperature. *Adv Appl Sci Res* 2011, **2**: 460–471.

[16] Rahman S, Nadeem K, Anis-Ur-rehman M, *et al*. Structural and magnetic properties of ZnMg-ferrite nanoparticles prepared using the co-precipitation method. *Ceram Int* 2013, **39**: 5235–5239.

[17] Choodamani C, Nagabhushana GP, Ashoka S, *et al*. Structural and magnetic studies of $Mg_{(1-x)}Zn_xFe_2O_4$ nanoparticles prepared by a solution combustion method. *J Alloys Compd* 2013, **578**: 103–109.

[18] Phor L, Kumar V. Self-cooling by ferrofluid in magnetic field. *SN Appl Sci* 2019, **1**: 1696.

[19] Mohammed KA, Al-Rawas AD, Gismelseed AM, *et al*. Infrared and structural studies of $Mg_{1-x}Zn_xFe_2O_4$ ferrites. *Physica B* 2012, **407**: 795–804.

[20] Kumari N, Kumar V, Singh SK. Effect of $Cr^{3+}$ substitution on properties of nano-$ZnFe_2O_4$. *J Alloys Compd* 2015, **622**: 628–634.

[21] Gul IH, Abbasi AZ, Amin F, *et al*. Structural, magnetic and electrical properties of $Co_{1-x}Zn_xFe_2O_4$ synthesized by co-precipitation method. *J Magn Magn Mater* 2007, **311**: 494–499.

[22] Globus A, Pascard H, Cagan V. Distance between magnetic ions and fundamental properties in ferrites. *J Phys Colloques* 1977, **38**: C1-163–C1-168.

[23] Mazen SA, Abdallah MH, Sabrah BA, *et al*. The effect of titanium on some physical properties of $CuFe_2O_4$. *Phys Stat Sol (a)* 1992, **134**: 263–271.

[24] Zaki HM, Al-Heniti SH, Elmosalami TA. Structural, magnetic and dielectric studies of copper substituted nano-crystalline spinel magnesium zinc ferrite. *J Alloys Compd* 2015, **633**: 104–114.

[25] Thakur P, Sharma R, Kumar M, *et al*. Superparamagnetic La doped Mn–Zn nano ferrites: Dependence on dopant content and crystallite size. *Mater Res Express* 2016, **3**: 075001.

[26] Levine BF. D-electron effects on bond susceptibilities and ionicities. *Phys Rev B* 1973, **7**: 2591.

[27] Phor L, Kumar V. Structural, magnetic and dielectric properties of lanthanum substituted $Mn_{0.5}Zn_{0.5}Fe_2O_4$. *Ceram Int* 2019, **45**: 22972–22980.

[28] Lakhani VK, Pathak TK, Vasoya NH, *et al*. Structural parameters and X-ray Debye temperature determination study on copper-ferrite-aluminates. *Solid State Sci* 2011, **13**: 539–547.

[29] Phor L, Kumar V. Structural, thermomagnetic, and dielectric properties of $Mn_{0.5}Zn_{0.5}Gd_xFe_{2-x}O_4$ ($x$ = 0, 0.025, 0.050, 0.075, and 0.1). *J Adv Ceram* 2020, **9**: 243–254.

[30] Waldron RD. Infrared spectra of ferrites. *Phys Rev* 1955, **99**: 1727.

[31] Chhantbar, MC, Trivedi UN, Tanna PV, *et al*. Infrared spectral studies of Zn-substituted $CuFeCrO_4$ spinel ferrite system. *Indian J Phys* 2004, **78A**: 321–326.

[32] Zaki HM, Dawoud HA. Far-infrared spectra for copper-zinc mixed ferrites. *Phys B: Condens Matter* 2010, **405**: 4476–4479.

[33] Modi KB, Trivedi UN, Sharma PU, *et al*. Study of elastic properties of fine particle-copper zinc ferrites through infrared spectroscopy. *Indian J Pure Ap Phy* 2006, **44**: 165–168.

[34] Chahal S, Rani N, Kumar A, *et al*. UV-irradiated photocatalytic performance of yttrium doped ceria for hazardous Rose Bengal dye. *Appl Surf Sci* 2019, **493**: 87–93.

[35] Priyadharsini P, Pradeep A, Rao PS, *et al*. Structural, spectroscopic and magnetic study of nanocrystalline Ni–Zn ferrites. *Mater Chem Phys* 2009, **116**: 207–213.

[36] Phor L, Kumar V. Self-cooling device based on thermomagnetic effect of $Mn_xZn_{1-x}Fe_2O_4$ ($x$ = 0.3, 0.4, 0.5, 0.6, 0.7)/ferrofluid. *J Mater Sci: Mater Electron* 2019, **30**: 9322–9333.

[37] Tholkappiyan R, Vishista K. Combustion synthesis of Mg–Er ferrite nanoparticles: Cation distribution and structural, optical, and magnetic properties. *Mater Sci Semicond Process* 2015, **40**: 631–642.

[38] Kumari N, Kumar V, Khasa S, *et al*. Chemical synthesis and magnetic investigations on $Cr^{3+}$ substituted Zn-ferrite

superparamagnetic nano-particles. *Ceram Int* 2015, **41**: 1907–1911.

[39] Mazen SA, Mansour SF, Zaki HM. Some physical and magnetic properties of Mg–Zn ferrite. *Cryst Res Technol* 2003, **38**: 471–478.

[40] Shinde TJ, Gadkari AB, Vasambekar PN. Magnetic properties and cation distribution study of nanocrystalline Ni–Zn ferrites. *J Magn Magn Mater* 2013, **333**: 152–155.

[41] Stoner EC, Wohlfarth EP. A mechanism of magnetic hystersis in hetrogeneous alloys. *Philos T R Soc A* **240,** 1948, **240:** 599–642.

[42] Bammannavar BK, Nair LR, Pujar RB, Chougule BK. Preparation, characterization and physical properties of Mg–Zn ferrites. *Indian J Eng Mater Sci* 2007, **14**: 381–385.

[43] Kumar V, Rana A, Yadav MS, *et al*. Size-induced effect on nano-crystalline $CoFe_2O_4$. *J Magn Magn Mater* 2008, **320**: 1729–1734.

[44] Thota S, Kashyap SC, Sharma SK, *et al*. Micro Raman, Mossbauer and magnetic studies of manganese substituted zinc ferrite nanoparticles: Role of Mn. *J Phys Chem Solids* 2016, **91**: 136–144.

[45] Montiel H, Alvarez G, Gutiérrez M, *et al*. Microwave absorption in Ni–Zn ferrites through the Curie transition. *J Alloys Compd* 2004, **369**: 141–143.

[46] Chu P, Mills DL, Arias R. Exchange/dipole collective spin-wave modes of ferromagnetic nanosphere arrays. *Phys Rev B* 2006, **73**: 094405.

[47] Schlömann E. Ferromagnetic resonance in polycrystalline ferrites with large anisotropy—I. *J Phys Chem Solids* 1958, **6**: 257–266.

[48] Schlömann E, Zeender JR. Ferromagnetic resonance in polycrystalline nickel ferrite aluminate. *J Appl Phys* 1958, **29**: 341–343.

[49] Srivastava C, Patni M. Ferromagnetic relaxation processes in polycrystalline magnetic insulators. *J Magn Reson 1969* 1974, **15**: 359–366.

[50] Yamashita T, Hayes P. Analysis of XPS spectra of $Fe^{2+}$ and $Fe^{3+}$ ions in oxide materials. *Appl Surf Sci* 2008, **254**: 2441–2449.

[51] Yan ZK, Gao JM, Li Y, *et al*. Hydrothermal synthesis and structure evolution of metal-doped magnesium ferrite from saprolite laterite. *RSC Adv* 2015, **5**: 92778–92787.

[52] Liu J, Zeng M, Yu RH. Surfactant-free synthesis of octahedral $ZnO/ZnFe_2O_4$ heterostructure with ultrahigh and selective adsorption capacity of malachite green. *Sci Rep* 2016, **6**: 25074.

[53] Guijarro N, Bornoz P, Prévot M, *et al*. Evaluating spinel ferrites $MFe_2O_4$ (M = Cu, Mg, Zn) as photoanodes for solar water oxidation: Prospects and limitations. *Sustainable Energy Fuels* 2018, **2**: 103–117.

[54] Dom R, Chary AS, Subasri R, *et al*. Solar hydrogen generation from spinel $ZnFe_2O_4$ photocatalyst: Effect of synthesis methods. *Int J Energy Res* 2015, **39**: 1378–1390.